

# AN EMISSION SURFACE APPROACH FOR NOISE PROPAGATION FROM HIGH SPEED SOURCES

L. Vendemini, L. Vigevano

Dipartimento di Scienze e Tecnologie Aerospaziali - Politecnico di Milano, Italy

## Abstract

The computer graphics algorithm of the *marching cubes* is adopted to compute the emission surface corresponding to a permeable Ffowcs Williams-Hawkings surface moving at arbitrary speeds. The algorithm is capable to successfully reconstruct the multiple disjoint surfaces generated by a transonic or supersonic motion of the source. A preliminary validation of the method, carried out for a two-blade rotor with simplified aerodynamic models, has given encouraging results.

## 1 Introduction

Nowadays, noise emissions from a helicopter rotor need to be carefully determined starting from the preliminary design phase. This is normally accomplished coupling the aerodynamic prediction tools with an integral propagation method. Starting from the Ffowcs Williams-Hawkings (FWH) equation, here schematized with the non homogeneous wave equation:

$$\square^2 \Phi(\mathbf{x}, t) = Q(\mathbf{x}, t) \delta(f)$$

the most popular time-domain methods to predict far-field noise propagation, like Farassat's 1A formulation<sup>1</sup> or Di Francescantonio's KFWH formulation<sup>2</sup>, make use of a retarded time approach, i.e.:

$$4\pi\Phi(\mathbf{x}, t) = \int_{f=0} \left[ \frac{Q(\mathbf{y}, \tau)}{r|1 - M_r|} \right]_{ret} dS$$

Using a permeable surface  $f(\mathbf{x}, t) = 0$  that include most of the noise sources, this approach allows to neglect the quadrupole source term still assuring a good accuracy of the results together with computational efficiency.

There are however contradictory requirements when coupling such methods with a CFD prediction of the aerodynamic field. On one hand, a stationary permeable surface which includes all the

rotating blades of the rotor is a optimal choice for the retarded time formulation, but requires a huge amount of computational resources to achieve high accuracy of the CFD solution far from the blades. On the other hand, a small and rotating permeable surface around each blade may be considered the optimal choice for the CFD simulation, but may prevent a reliable prediction of noise due to the Doppler singularity of the retarded time formulation.

A different formulation, which can be used for any speed of the noise source, is that based on the *emission surface*  $F(\mathbf{x}, t) = 0$ <sup>1</sup> :

$$4\pi\Phi(\mathbf{x}, t) = \int_{F=0} \frac{1}{r} \left[ \frac{Q(\mathbf{y}, \tau)}{\Lambda} \right]_{ret} d\Sigma$$

with  $\Lambda = |\nabla F|$ , which avoids the Doppler singularity. The emission surface  $F = 0$  represent the locus of the points, belonging to the surface  $f = 0$ , from which perturbations are generated that simultaneously reach the observer at a given time instant  $t$ . This formulation has not been used very often in the past, due to the the complexity and the computational effort needed to numerically reconstruct the surface  $F = 0$ . At present, only two algorithms were proposed in the literature: the K-algorithm of Ianniello<sup>3,4</sup> and the marching cubes algorithm of Brentner<sup>5</sup>.

This paper describes an implementation of the emission surface formulation using the marching cube approach. The proposed method is verified against analytical solutions for simple noise

sources, to show how the numerical error is influenced by the frequency of the noise source and by the dimension and the shape of the permeable surface selected. Results are then shown for a pulsating sphere moving at subsonic, transonic and supersonic speeds, to demonstrate the capability of the approach at different source speeds. Finally, the proposed method is employed to predict the noise emitted from a two-blade rotor, using a simplified calculation of the blade aerodynamic loads, taken from<sup>6</sup>.

## 2 The permeable emission surface formulation

Considering a moving, permeable surface  $f(\mathbf{x}, t) = 0$ , with outward unit normal  $\nabla f = \hat{\mathbf{n}}$ , and using generalized derivatives, it is possible to formulate<sup>1, 2</sup> a general form of the FWH equation as:

$$\begin{aligned} \bar{\square}^2 p' &= \frac{\bar{\partial}}{\partial t} \{ [\rho_0 u_n + (\rho - \rho_0)(u_n - v_n)] \delta(f) \} \\ &- \frac{\bar{\partial}}{\partial x_i} \{ [P'_{ij} \hat{n}_j + \rho u_i (u_n - v_n)] \delta(f) \} + \\ &\frac{\bar{\partial}^2}{\partial x_i \partial x_j} [T_{ij} H(f)] \end{aligned} \quad (1)$$

with  $p'$  acoustic pressure,  $\rho$  fluid density,  $u_n = u_i \hat{n}_i$  fluid velocity normal to the surface,  $v_n = -\partial f / \partial t$  velocity of the surface,  $c$  speed of sound,  $T_{ij} = (\rho u_i u_j + P_{ij} - c_0^2 (\rho - \rho_0) \delta_{ij})$  the Lighthill tensor,  $P_{ij}$  the compressive stress tensor,  $P'_{ij} = P_{ij} - p_0 \delta_{ij}$ ,  $H(f)$  the Heaviside function,  $\bar{\square}^2 = \partial^2 / \partial t^2 - c_0^2 \partial^2 / \partial x_i^2$  the generalized wave operator. The notation  $\bar{\partial}$  indicates generalized derivatives while the subscripts 0 and  $n$  refers to undisturbed quantities and to quantities projected in direction  $\hat{\mathbf{n}}$ .

A more standard form of the FWH equation may be obtained introducing Di Francescantonio's notation<sup>2</sup>, defining:

$$\begin{aligned} U_i &= u_i + \left[ \left( \frac{\rho}{\rho_0} \right) - 1 \right] (u_i - v_i) \quad , \\ L_{ij} &= P'_{ij} + \rho u_i (u_j - v_j) \end{aligned} \quad (2)$$

so that equation eq.1 may be rewritten as:

$$\begin{aligned} \bar{\square}^2 p' &= \frac{\bar{\partial}}{\partial t} \{ [\rho_0 U_n] \delta(f) \} - \frac{\bar{\partial}}{\partial x_i} \{ [L_{ij} \hat{n}_j] \delta(f) \} + \\ &\frac{\bar{\partial}^2}{\partial x_i \partial x_j} [T_{ij} H(f)] \end{aligned} \quad (3)$$

The integral forms of eq. (3) are referred to as the retarded time, collapsing sphere and emission surface forms<sup>1</sup>. As already mentioned, the emission surface represents the locus of points of the control surface  $F(\mathbf{x}, t) = 0$  from which perturbations are emitted that reach the observer at the same time instant  $t$ , or:

$$F(\mathbf{y}; \mathbf{x}, t) = f(\mathbf{y}, t - \frac{r}{c_0}) = [f(\mathbf{y}, \tau)]_{ret} = 0$$

with  $\tau = t - \frac{r}{c_0}$  retarded time,  $r(\mathbf{x}, t; \mathbf{y}, \tau) = |\mathbf{x} - \mathbf{y}|$  and  $(\mathbf{x}, t)$ ,  $(\mathbf{y}, \tau)$  the space-time coordinates of the observer and the noise source. Such an emission surface is not necessarily a single connected surface: for supersonic sources, for instance, the multiple emission times cause the occurrence of unconnected patches, and this introduces some difficulties in the numerical computation of the surface itself.

The permeable emission surface formulation reads:

$$\begin{aligned} 4\pi p'(\mathbf{x}, t) &= \frac{1}{c_0} \frac{\partial}{\partial t} \int_{\Sigma} \left[ \frac{\rho_0 c_0 U_n + L_{nr}}{r \Lambda} \right]_{ret} d\Sigma + \\ &\int_{\Sigma} \left[ \frac{L_{nr}}{r^2 \Lambda} \right]_{ret} d\Sigma \end{aligned} \quad (4)$$

with  $\Lambda = |\nabla F| = \left[ \sqrt{1 - 2M_n \hat{\mathbf{n}} \cdot \hat{\mathbf{r}} + M_n^2} \right]_{ret}$ ,  $\hat{\mathbf{r}}$  unit vector in the radiation direction and the subscript  $r$  refers to quantities projected in direction  $\hat{\mathbf{r}}$ . The quadrupole terms have been neglected assuming that the control surface  $f = 0$  fully includes the noise sources.

Equation (4) may still present a singularity when  $\Lambda = 0$ , although less severe than the Doppler singularity. The reader is referred to<sup>4</sup> for a thorough discussion on this matter.

## 3 The marching cube algorithm

The Marching Cube (MC) method is an algorithm used in Computer Graphics to reconstruct accurately three-dimensional surfaces from a scalar 3D

field, proposed by Lorensen and Cline<sup>7</sup> in 1987. The method was adopted by Brentner<sup>5</sup> to the computation of the emission surface by adopting a source-time-dominant approach: the source time is chosen and the corresponding observer time is computed at each point of the control surface  $f = 0$ . By defining a structured grid on the control surface and successive slices for each selected source time, a 3D structured grid made of “cubes” is constructed, as in fig. 1 The emission surface  $F = 0$  is by definition an isosurface of this 3D field of observer times. In this paragraph we will give some details of the algorithm.

Every cube is defined by the  $i, j$  indexes of the control surface grid and the index  $k$  of the slice, for a total of  $N_i, N_j, N_k$  grid points. A global num-

bering  $Ind$  of the cube vertices is defined, see an example in Fig. 2. An analogous numbering is defined for the cube themselves and for the cube edges. The global numbering  $Ind$  of the cube vertices is connected to a local numbering  $V1\dots V8$  of the eight vertices of the generic cube through:

$$\begin{aligned} Ind(V2) &= Ind(V1) + 1 \\ Ind(V3) &= Ind(V2) + N_j \\ Ind(V4) &= Ind(V3) - 1 \\ Ind(V5) &= Ind(V1) + N_i \times N_j \\ Ind(V6) &= Ind(V2) + N_i \times N_j \\ Ind(V7) &= Ind(V3) + N_i \times N_j \\ Ind(V8) &= Ind(V4) + N_i \times N_j \end{aligned}$$

2

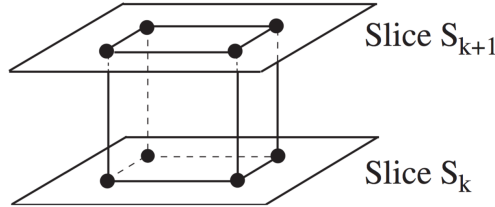


Figure 1: Generation of a cube

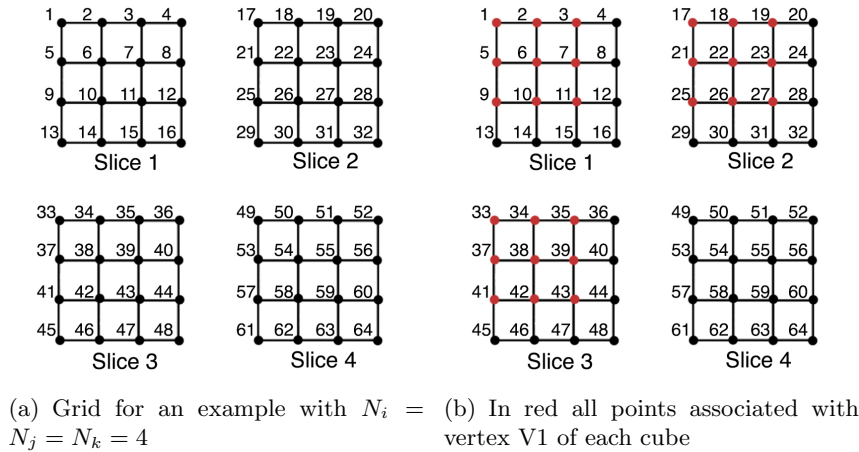


Figure 2: Example of vertex numbering

The connectivity between vertex numbering and cube numbering is done by associating the global vertex number corresponding to  $V1$ ,

$Ind(V1)$ , to the global cube number  $ID$ , as in table 1.

Assuming that the observer times  $t(\mathbf{x}, \mathbf{y}, \tau) =$

ID	Ind(V1)	Ind(V2)	Ind(V3)	Ind(V4)	Ind(V5)	Ind(V6)	Ind(V7)	Ind(V8)
<b>1</b>	<b>1</b>	2	6	5	17	18	22	21
<b>7</b>	<b>9</b>	10	14	13	25	26	30	29
<b>17</b>	<b>26</b>	27	31	30	42	43	47	46

Table 1: Example of cube-vertex connectivity

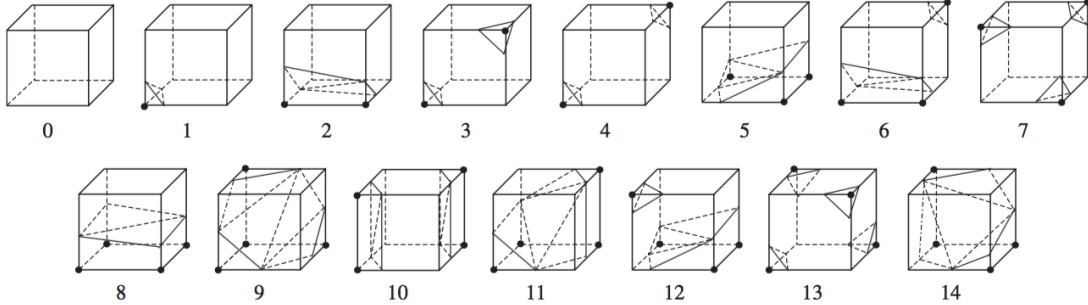


Figure 3: Topological cases considering rotation, reflexion and mirroring

$\tau + \frac{r(\mathbf{x}, \mathbf{y}, \tau)}{c_0}$  were computed for each grid point, the iso-surface at  $t = \bar{t} = const$  is built in successive steps. Firstly, each vertex is assigned the label 0 if  $t < \bar{t}$  or 1 otherwise; the iso-surface will intersect a cube edge only if the corresponding edges have different values. The cubes are then labelled as active if at least one edge contains an intersection. The possible combination of vertex labels for one active cube are 256 ( $2^8$ ) which reduces to 15, shown in fig. (3), by considering all possible symmetries. These are stored in a lookup table using a binary number conversion, which allow a direct identification of the intersected edges. The location of the intersection points  $V_{in}$  at the cube edge is computed by linear interpolation. The last step is the formation of the iso-surface with the triangles formed by the intersection points  $V_{in}$  (see fig. 3).

The original Lorensen and Cline<sup>7</sup> model is not consistent, however. It may results in the creation of holes in the iso-surface, due to interface ambiguity. Among different methods, proposed in the literature to resolve this ambiguity<sup>8</sup>, we selected that suggested by Montani *et al*<sup>9</sup> which directly modifies the lookup table, thus retaining the efficiency of the algorithm.

In applying the MC algorithm to the calculation of the emission surface, the control surface

$f = 0$  is parametrized as

$$\begin{aligned} x &= X(\xi, \eta, \tau) \\ y &= Y(\xi, \eta, \tau) \\ z &= Z(\xi, \eta, \tau) \end{aligned}$$

so that the MC grid is discretized in  $\xi, \eta, \tau$ . The parametrization allows to directly compute the triangle area  $\Delta\Sigma$ , surface velocity  $v$  and normal vector  $\hat{\mathbf{n}}$ . In addition to the observer time  $t$ , at the grid vertices are assigned the flow quantities  $\rho, p, \mathbf{u}$ , which are then linearly interpolated at the intersections. All quantities are arithmetically averaged over each triangle to perform the integration over the emitting surface.

Rewriting equation (4) as

$$4\pi p'(\mathbf{x}, t) = \frac{1}{c_0} \frac{\partial}{\partial t} (I_1) + I_2 \quad (5)$$

with

$$\begin{aligned} I_1 &= \int_{\Sigma} \left[ \frac{\rho_0 c_0 U_n + L_{nr}}{r\Lambda} \right]_{ret} d\Sigma \\ &= \int_{\Sigma} \left[ \frac{Q_1(\mathbf{y}, t - r/c_0)}{r\Lambda} \right]_{ret} d\Sigma \\ I_2 &= \int_{\Sigma} \left[ \frac{L_{nr}}{r^2\Lambda} \right]_{ret} d\Sigma \\ &= \int_{\Sigma} \left[ \frac{Q_2(\mathbf{y}, t - r/c_0)}{r^2\Lambda} \right]_{ret} d\Sigma \end{aligned}$$

having assumed constant approximation in each triangle, we may obtain the value of the integrals by direct summation over all triangles that compose the emission surface as

$$I_1 = \sum_{i=1}^{N_{tri}} \left[ \frac{Q_1(\mathbf{y}_i, t - r_i/c_0)}{r_i \Lambda_i} \right]_{ret} \Delta \Sigma_i$$

$$I_2 = \sum_{i=1}^{N_{tri}} \left[ \frac{Q_2(\mathbf{y}_i, t - r_i/c_0)}{r_i^2 \Lambda_i} \right]_{ret} \Delta \Sigma_i$$

while the time derivative of  $I_1$  is obtained with a centered finite difference over the observer time evaluations.

## 4 Algorithm validation

### 4.1 Surface reconstruction

The implemented MC algorithm was first verified in terms of its capability of reconstructing complex 3D surfaces using different grid discretizations. We report here as an example the reconstruction of three types of surfaces:

- **Surface 1**

Evaluation domain:  $x \in [-1, 1], y \in [-1, 1], z \in [-1, 1]$ .

$$f_1(x, y, z) = \sqrt{x^2 + y^2 + z^2} - 1 \quad (6)$$

Being this surface a sphere of unit radius, the value of the area is  $S_1 = 4\pi$ .

- **Surface 2**

Evaluation domain:  $x \in [-6, 6], y \in [-2, 2], z \in [-4, 10]$ .

$$f_2(x, y, z) = \left(3 - 3x\right)^2 e^{-x^2 - (y+1)^2}$$

$$- 10 \left(\frac{x}{5} - x^3 - y^5\right) e^{-x^2 - y^2}$$

$$- \frac{1}{3} e^{-(x+1)^2 - y^2} - z \quad (7)$$

The integral to compute the area  $S_2$  has to be numerically approximated, with a converged value of  $S_2 = 118.05$ .

- **Surface 3**

Evaluation domain:  $x \in [-3, 3], y \in [-4, 4], z \in [-40, 40]$ .

$$f_3(x, y, z) = \left(1 - \left(\frac{x}{6}\right)^2 - \left(\frac{y}{3.5}\right)^2\right)$$

$$\left(\left(x - 3.9\right)^2 + y^2 - 1.44\right)$$

$$\left(x^2 + y^2 - 1.44\right) \left(\left(x + 3.9\right)^2\right.$$

$$\left. + y^2 - 1.44\right) - z^2 \quad (8)$$

$S_3$  may be computed analytically in this case, with  $S_3 = 3150.03$ .

The quality of the MC reconstruction is evaluated from the ratio of the computed area to the exact area,  $\eta = S_{MC}/S_E$  over grids with  $N_i = N_j = N_k = n$ . The efficiency of the algorithm is assessed by computing the ratio between the number of formed triangles to the number of cubes of the grid. The obtained surfaces are shown in fig. 4, for coarse and fine grids. Observing fig. 5 we can notice that for all three cases convergence ( $\eta \in [0.9, 1]$ ) is achieved for  $n = 30$ , corresponding to a grid of 27000 points.

### 4.2 Stationary control surface

The next step is to validate the method with some non realistic test cases with different analytical noise sources. This exercise will also allow to assess the MC discretization effects and the size and shape of the control surface.

We begin considering a steady spherical permeable surface, centered on a point noise source. The analytical solutions for monopole, dipole and quadrupole may be used to associate the values of acoustic pressure and velocity on the permeable surface. The sphere is uniformly discretized using cylindrical coordinates  $\theta$  and  $z$ , with  $N_\theta = N_z = n$  points, and may have different radius, from  $r_s = 0.5$  m to  $r_s = 5.5$  m. The number of slices selected to generate the MC is varied according to the source frequency, to avoid aliasing errors.

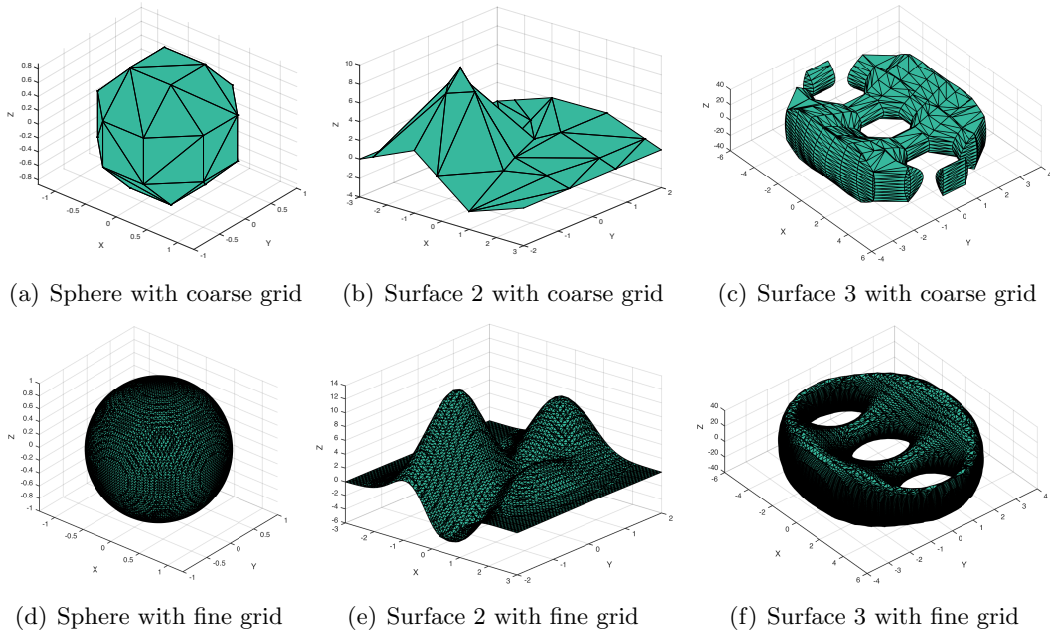


Figure 4: Reconstruction of test surfaces

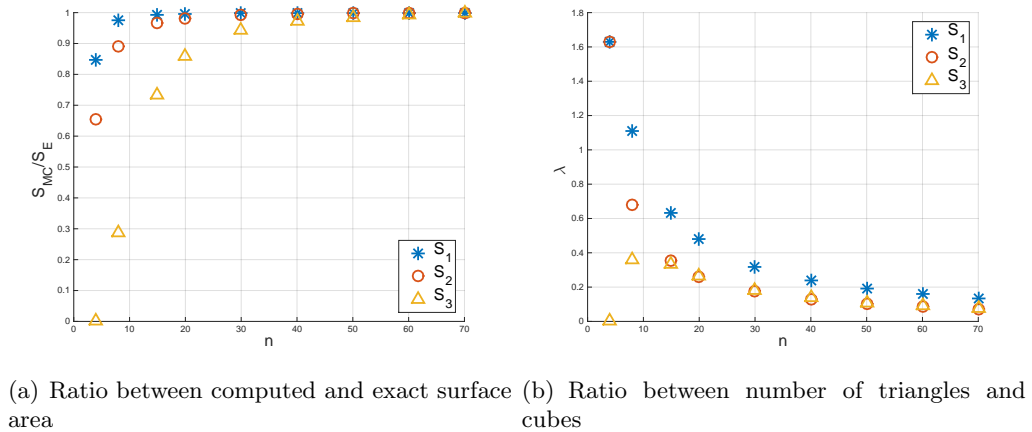


Figure 5: Convergence of MC method

2

The emitting surface obviously coincides with the control surface when the latter is still. The difference between the analytical and numerical solutions is measured in terms of a global parameter  $\varepsilon$  defined as

$$\varepsilon = \frac{\sum_{l=1}^{N_t} \sum_{m=1}^{N_x} |p'(\mathbf{x}_m, t_l) - p'_{ex}(\mathbf{x}_m, t_l)|}{\sum_{l=1}^{N_t} \sum_{m=1}^{N_x} |p'_{ex}(\mathbf{x}_m, t_l)|}$$

with  $p'_{ex}$  the exact solution, and  $N_t = 1$ ,  $N_x = 240$ , respectively, the number of temporal and spatial observations carried out, the latter obtained for observer positions located on a sphere with radius  $r_{obs} = 30$  m.

Results for different values of  $n$ ,  $r_s$  and emission frequency for a monopole source are shown in fig. 6. Convergence of the numerical solution decreases with increasing frequency of the monopole. At a given frequency, convergence is improved by reducing the radius of the control sphere. Similar observations may also be drawn using dipole

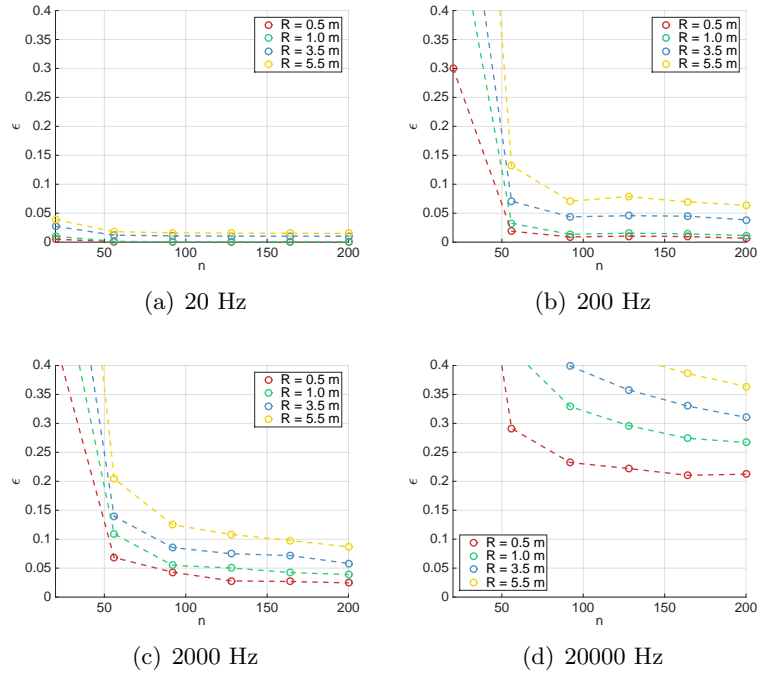


Figure 6: Global error for the still control sphere, monopole source

and quadrupole sources. As an example of the simulation of a complex source, fig. 7 shows the analytical and numerical signals for an observer located at  $r = 30$  m in the  $x - y$  horizontal plane.

Similar results are obtained using a cylindrical control surface. It is worth noting that the algorithm allows to describe the control surface as a collection of independent surfaces: for the cylinder case, the permeable surface is composed by the two bases and the surface of revolution.

### 4.3 Moving control surface

The last non realistic validation case considers a rotating monopole source surrounded by a spherical control surface moving with it. The source rotates in the  $x - y$  plane at a distance  $d = 3$  m from the origin of the coordinate system, with different angular velocities, see table 2. The radius of the control surface is  $r_s = 0.5$  m. The observer is located at  $\mathbf{x} = [4, 0, 0]$  m for all cases. The surface discretization of the control surface is again uniform, with  $N_i = N_j = N_\theta = N_z = 80$ , a value which assure convergence of the results for the monopole frequency of 100 Hz and the small value of  $r_s$  considered. The only discretization parameter that is varied is the number of temporal slices  $N_k = n_\tau$ , ranging from 20 to 220.

#### 4.3.1 Subsonic motion

When the control surface motion is fully subsonic, there exists a single emission surface, although not coincident with the sphere, see fig. 8. In the figure, the emission surface is colored with the value of the emission time. The local Mach number range for this case is  $0.46 \leq M \leq 0.65$ , but the relevant value to compute the noise propagated from the emission surface is the local Mach number *normal* to the surface,  $M_n$ , the maximum value of which  $M_{n,max} = 0.55$  is reported in table 2. The effect of increasing the number of temporal slices is shown in fig. 9(a), where the acoustic pressure, non dimensionalized with its maximum value, is plotted for one revolution of the source. The figure demonstrates a converged result for  $n_\tau = 60$ . Figure 9(b) reports, during one revolution, the value of the emission surface area, normalized with its maximum value: since the period shown starts when the source is located at the closest position to the observer, the area decreases when the source is moving away from the observer and increases when moving closer to the observer. Finally, to assess the possibility that the local value of  $\Lambda$  becomes close to zero, figure 9(c) displays the value of  $(1/\Lambda)_{max}$ : for subsonic motion the kernels of the acoustic integrals remain regular for all the rotation period.

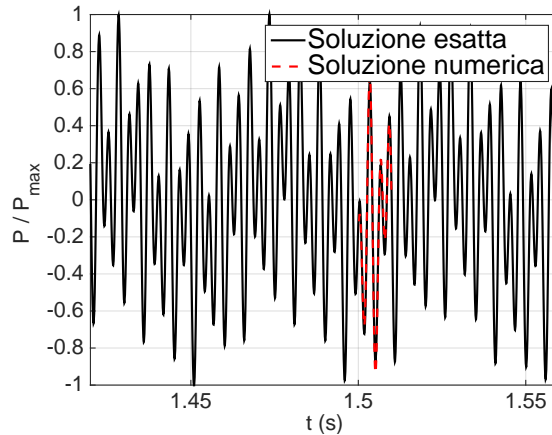


Figure 7: Noise source made of a monopole at 20 Hz, a dipole at 200 Hz and a quadrupole at 300 Hz (black: analytical; red: numerical)

case	subsonic	transonic	supersonic
$\omega$ (rad/s)	62.83	157	377
$M_{n,max}$ (m/s)	0.55	1.385	3.33

Table 2: Rotating source operating parameters

2

#### 4.3.2 Transonic motion

In this operating condition the angular velocity of the control surface is increased such as to locally reach a value  $M_{n,max} > 1$ . The emission surface at some instant of time during one revolution is composed of two separate surfaces, as seen in fig. 10, where the yellow one, which indicates less retarded emission times, is located closer to the observer. The evolution of the non dimensional pressure (fig. 11(a)) evidences that a value of  $n_\tau = 80$  is needed for convergence, although the emission surface area value converges with a coarser MC grid (fig. 11(b)). The singularity term  $(1/\Lambda)_{max}$  increases of one order of magnitude with respect to the previous case (fig. 11(c)).

#### 4.3.3 Supersonic motion

The last case reaches a maximum value of the normal Mach number as high as 3.33. It has clearly a limited practical meaning, but it is meant as a severe test case for the capability of the algorithm to reconstruct the emission surface when this is composed of several disjoint parts. As seen in fig. 12, the emission surface at some instant is composed

of three separate surfaces. The computational requirements in terms of number of slices required for the MC grid become high: fig. 13 shows that convergence is not fully reached for  $n_\tau = 220$ . The first part of the period, when the emitting surface splits from two to three parts, is where the differences among discretizations are more evident. It is worth noting that the singular behavior of this supersonic case is no worse than that of the transonic case (fig. 13(c)).

## 5 A rotor application

As a preliminary rotor validation case we consider the two-blade, fully articulated, twisted, NACA0012 rotor with radius  $R = 1.829$  m, used by Brentner<sup>6</sup> for the validation of the WOPWOP code. Being the aerodynamic pressure assigned on the blade themselves, the general porous formulation (4) needs to be specialized to the case in which the control surface  $f(\mathbf{x}, t) = 0$  is a solid surface. Being  $(u_n - v_n) = 0$  it results:

$$4\pi p'(\mathbf{x}, t) = \frac{1}{c_0} \frac{\partial}{\partial t} \int_{\Sigma} \left[ \frac{\rho_0 c_0 v_n + \tilde{p} \hat{\mathbf{n}} \cdot \hat{\mathbf{r}}}{r\Lambda} \right]_{ret} d\Sigma + \int_{\Sigma} \left[ \frac{\tilde{p} \hat{\mathbf{n}} \cdot \hat{\mathbf{r}}}{r^2 \Lambda} \right]_{ret} d\Sigma + p'_Q(\mathbf{x}, t) \quad (9)$$

with  $\tilde{p} = p - p_0$  the gauge pressure on the blade surface. In principle, the quadrupole term  $p'_Q(\mathbf{x}, t)$  cannot be neglected, but it will not be considered in the following.

The pressure distribution on the blade surface is computed using a combination of Blade Element-Momentum theory (BEM) and analytic airfoil theory, and the blade kinematics is prescribed up to the second harmonics<sup>6</sup>. The control surface is described as the sum of four surfaces, i.e. upper and lower surfaces for the two blades, thanks to the generality of the method. The surface discretization is uniform in spanwise direction, while non uniform in chordwise direction. Since the calculation of the blade position, normal vector and velocity from the assigned kinematics implies several matrix products, to make the algorithm more computationally efficient these quantities are computed at the MC vertices for one blade revolution and stored. Their values at the vertices of the triangles of the emission surface is then interpolated from the stored table, together with the gauge pressure  $\tilde{p}$ .

Results are compared with experimental data and WOPWOP calculations for a test case with advance ratio  $\mu = 0.207$  and  $M_{tip} = 0.73$ . Two different observers are considered, both moving with the same translational velocity of the rotor: the first observer is located ahead of the rotor, at a fixed distance from the rotor hub, non dimensionalized with the rotor radius, of  $\Delta \mathbf{x}_{O_1} = [1.381, -1.181, -0.016]$ , laying approximately in the rotor plane; the second observer is located at  $\Delta \mathbf{x}_{O_2} = [0.661, -1.181, -1.804]$ , i.e. below the rotor disk. At observer  $O_1$ , one can expect a signal dominated by a negative acoustic pressure peak periodic in time, due to the prevalent thickness noise contribution; at the second observer  $O_2$ , on the contrary, one can expect a prevailing loading noise contribution.

The computed results, shown in fig. 14, confirm these expectations, as can be evidenced by separating the thickness and loading noise contributions.

In fig. 15 are reported the emission surfaces at three different observer times for observer  $O_1$ , corresponding approximately to the positive peak, the negative peak and the end of recompression in the pressure-time history of fig. 14(a). It is possible to notice that to the advancing blade, which has a larger velocity, corresponds an emission surface  $\Sigma$  more deformed with respect to that generated by the retreating blade.

The comparison of the results obtained with the present method for observer  $O_1$  with the available experimental data and the WOPWOP results, fig. 16, shows a reasonable agreement.

## 6 Conclusions

Following Brentner<sup>5</sup>, the computer graphics algorithm of the *marching cubes* has been adopted to compute the emission surface corresponding to a permeable FW-H surface moving at arbitrary speeds. The reconstruction of analytical surfaces has been used to verify the basic MC algorithm. Numerical simulations of non realistic stationary and moving source test cases have allowed to validate the proposed emission surface method and to assess the influence of the discretization parameters on the achieved results. The method proved capable to successfully reconstruct the multiple disjoint surfaces generated by a transonic or supersonic motion of the source. The proposed approach is then applied to the noise prediction from a two-blade rotor, using simplified aerodynamic models. A limited comparison with experimental data and numerical results from the WOPWOP code gives encouraging results.

*Copyright Statement:* The authors confirm that they, and/or their company or organization, hold copyright on all of the original material included in this paper. The authors also confirm that they have obtained permission, from the copyright holder of any third party material included in this paper, to publish it as part of their paper. The authors confirm that they give permission, or have obtained permission from the copyright holder of this paper, for the publication and distribution of this paper as part of the ERF2017 proceedings or as individual offprints from the proceedings and for inclusion in a freely accessible web-based repository.

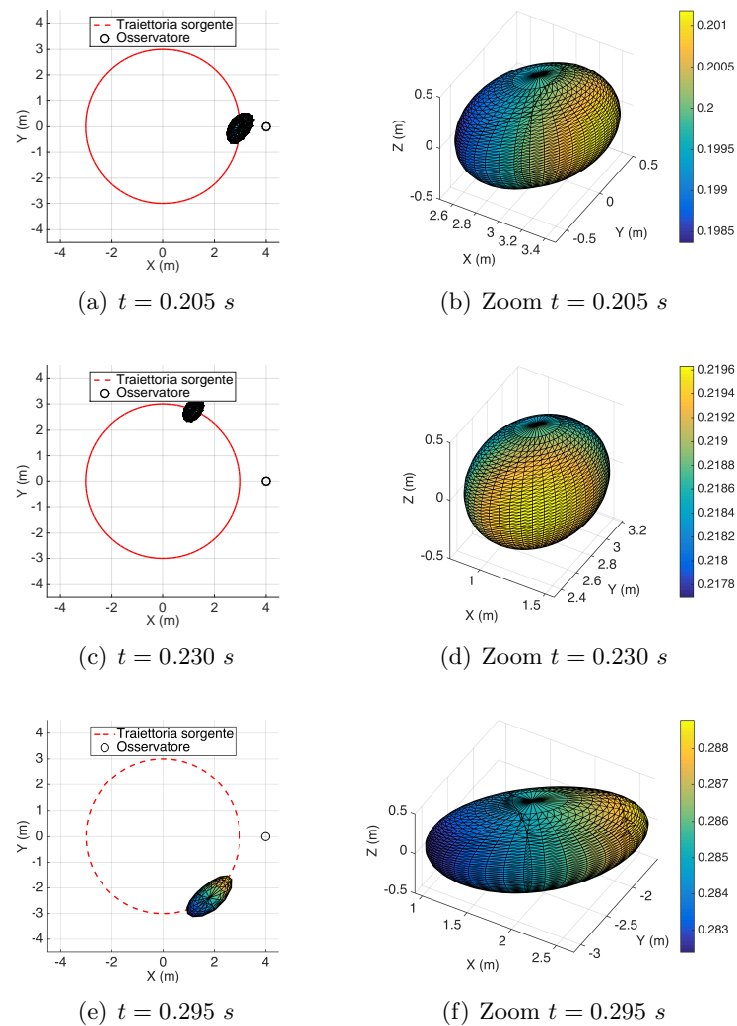


Figure 8: Subsonic motion

## References

- [1] K. S. Brentner and F. Farassat. Modeling aerodynamically generated sound of helicopter rotors. *Progr. in Aerospace Sciences*, 39:83–120, 2003.
- [2] P. di Franciscantonio. A new boundary integral formulation for the prediction of sound radiation. *J. of Sound and Vibration*, 202:491–509, 1997.
- [3] S. Ianniello. Algorithm to integrate the Ffowcs Williams-Hawkings equation on supersonic rotating domain. *AIAA J.*, 37:1040–1047, 1999.
- [4] S. Ianniello. New perspectives in the use of the Ffowcs Williams-Hawkings equation for aeroacoustic analysis of rotating blades. *J. of Fluid Dynamics*, 570:79–127.
- [5] K. S. Brentner. A new algorithm for computing acoustic integrals. In *Proceedings of the IMACS 14th World Congress on Computational and Applied Mathematics*, volume 2, pages 592–595, 1994.
- [6] K. S. Brentner. Prediction of helicopter rotor discrete frequency noise. In *NASA Technical Memorandum 87721*, 1986.
- [7] W. E. Lorenson and H. E. Cline. Marching Cubes: a high resolution 3D surface construction algorithm. *Comput. Graphics*, 21:163–169.
- [8] T. S. Newman and H. Yi. A survey of the marching cubes algorithm. *Computers and Graphics*, 30:854–879.
- [9] C. Montani, R. Scateni, and R. Scopigno. A modified look-up table for implicit disambiguation of Marching Cubes. *The Visual Computer*, 10:353–355.

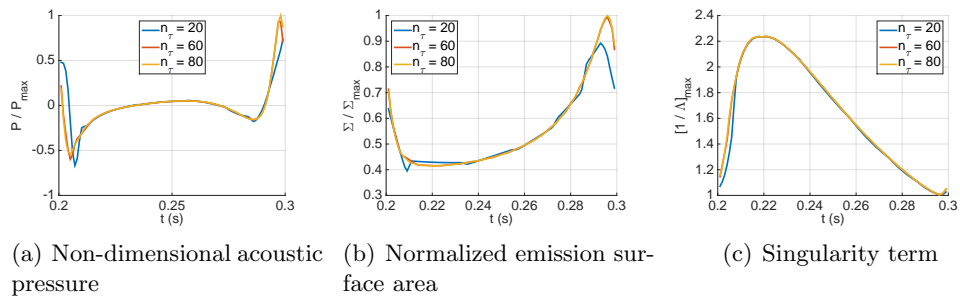


Figure 9: Convergence analysis for the subsonic motion

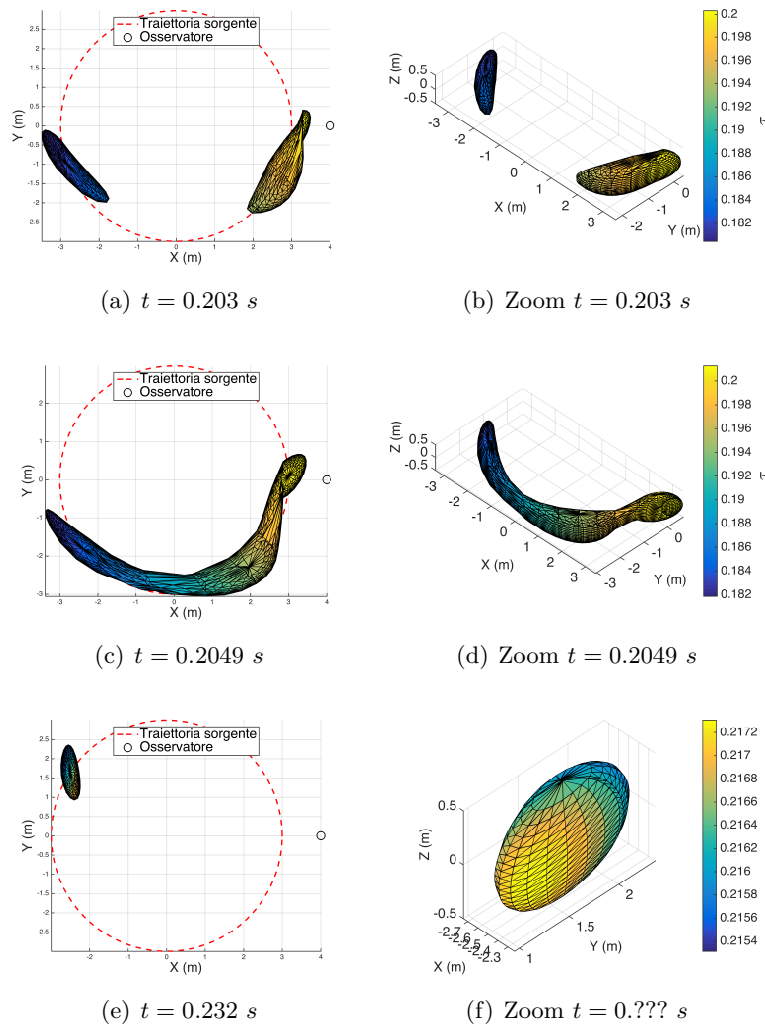


Figure 10: Transonic motion

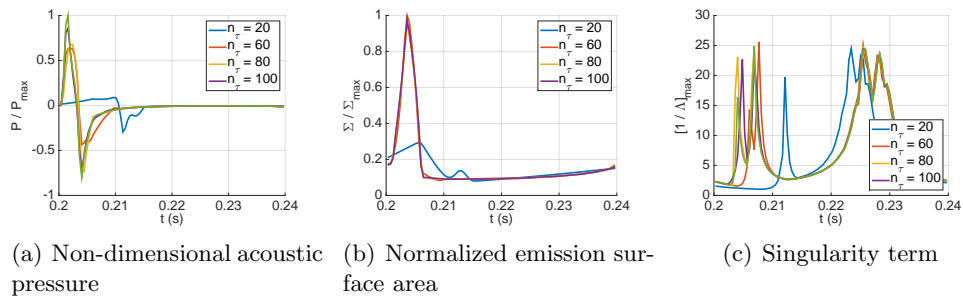


Figure 11: Convergence analysis for the transonic motion

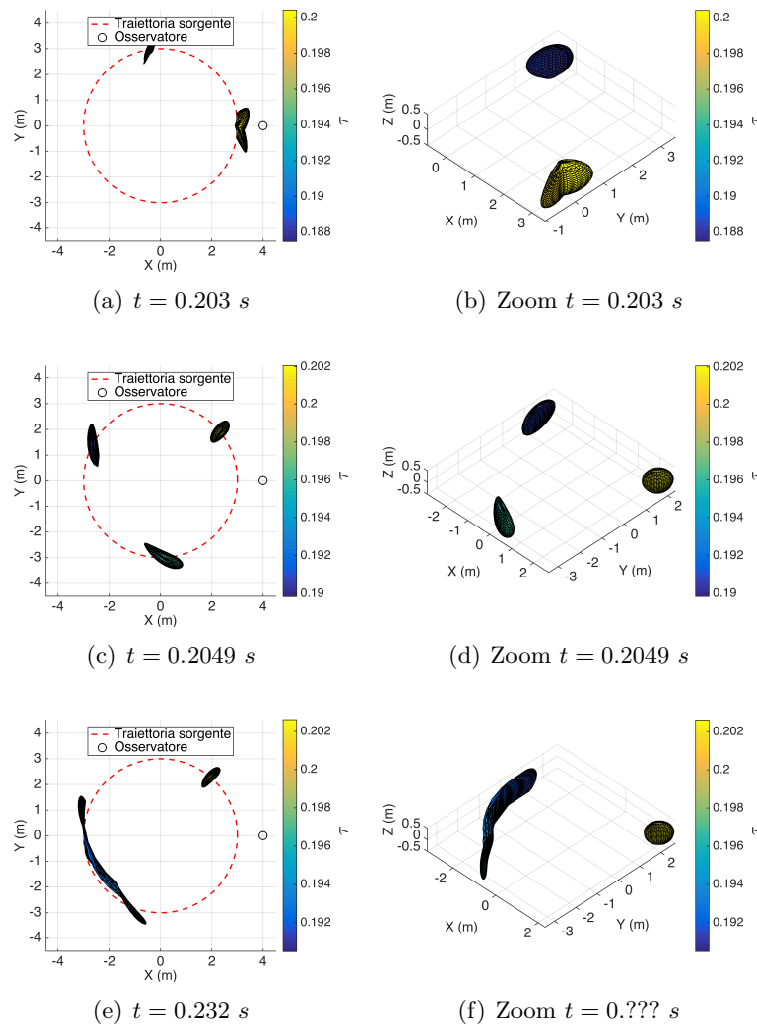


Figure 12: Supersonic motion

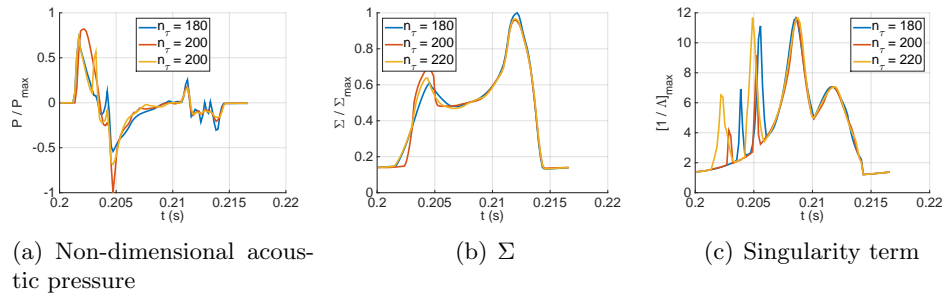


Figure 13: Convergence analysis for the supersonic motion

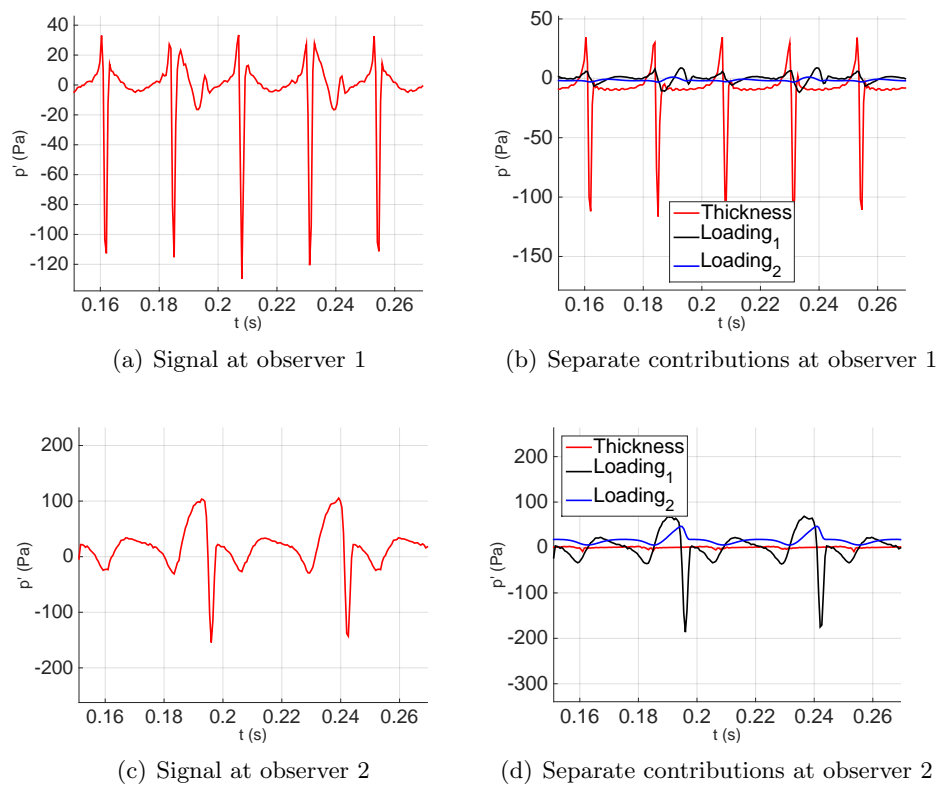


Figure 14: Acoustic pressure at the two observers

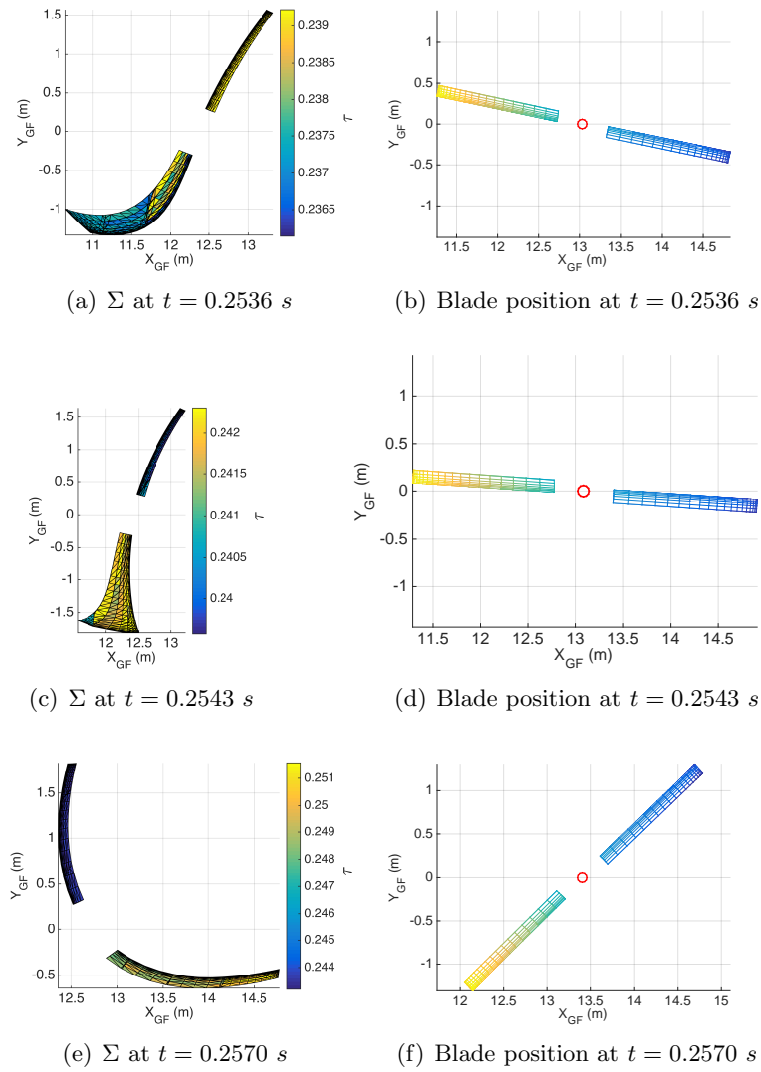


Figure 15: Emission surface for observer 1

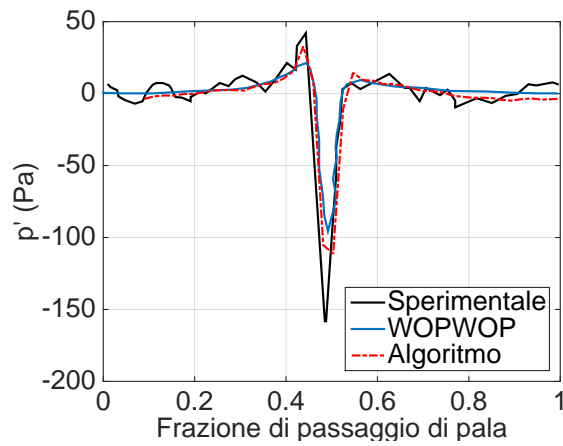


Figure 16: Comparison of results